HHS Public Access

Author manuscript

Optica. Author manuscript; available in PMC 2021 September 08.

Published in final edited form as:

Optica. 2019 April 20; 6(4): 389–395. doi:10.1364/optica.6.000389.

Video-rate large-scale imaging with Multi-Z confocal microscopy

Amaury Badon[1,*], **Seth Bensussen**[1], **Howard J. Gritton**[1], **Mehraj R. Awal**[2], **Christopher V. Gabel**[2,3], **Xue Han**[1,3], **Jerome Mertz**[1,3]

[1]Department of Biomedical Engineering, Boston University, Boston, Massachusetts 02215, USA

[2]Department of Physiology and Biophysics, Boston University School of Medicine, Boston, Massachusetts 02218, USA

[3]Boston University Photonics Center, Boston, Massachusetts 02215, USA

Abstract

Fast, volumetric imaging over large scales has been a long-standing challenge in biological microscopy. To address this challenge, we report an augmented variant of confocal microscopy that uses a series of reflecting pinholes axially distributed in the detection space, such that each pinhole probes a different depth within the sample. We thus obtain simultaneous multiplane imaging without the need for axial scanning. Our microscope technique is versatile and configured here to provide two-color fluorescence imaging with a field of view larger than a millimeter at video rate. Its general applicability is demonstrated with neuronal imaging of both *Caenorhabditis elegans* and mouse brains *in vivo*.

1. INTRODUCTION

Recently, there has been a trend toward the development of microscopy systems that can monitor cellular activity over large spatial scales with high temporal resolution. General conditions for such imaging are that the microscope provide enough spatial resolution to distinguish individual cells and enough temporal resolution to accurately track the sample dynamics of interest. Moreover, to monitor large populations of cells *in vivo*, volumetric imaging is required, ideally encompassing hundreds to thousands of individual cells. The confluence of these conditions poses a challenge [1,2]. Many previous approaches have been developed for volumetric imaging. For example, widefield microscopes benefit from the large sensor areas and excellent spatiotemporal resolution of modern cameras and provide single-shot 2D imaging. Volumetric imaging at high speed can then be achieved with fast axial scans [3–5] or instantaneously using wavefront coding [6,7], diffractive elements [8–10], or light-field approaches [11,12]. However, lack of optical sectioning makes these approaches susceptible to background (and its attendant noise), limiting them to shallow depths, sparse samples, or a reliance on intensive numerical postprocessing that requires *a priori* sample information. Light-sheet [13,14] or targeted illumination [15] improves sectioning by reducing out-of-focus excitation but similarly suffers from an

*Corresponding author: badon.amaury@gmail.com.

inability to prevent scattered background light from impinging the camera sensor, yielding limited image contrast in thick tissue such as mouse brain. Alternatively, higher contrast in thick tissue can be obtained with scanning techniques involving multiphoton excitation or confocal detection. For example, multiplane imaging has been achieved with two-photon microscopy using spatiotemporal multiplexing of the excitation beam [16,17].

However, scanning microscopes are generally operated with micron-scale resolution, causing them to be slow and to produce massive amounts of data when operated over large fields of view or to be limited to modest volumes [18]. Random access techniques [19,20] reduce the amounts of data production but require scan precalibration and are sensitive to motion artifacts. Alternatively, data production can be reduced by purposefully limiting the spatial resolution, either axially [21,22] (though see [23–25], where axial resolution can be recovered in sparse samples by postprocessing) or near-isotropically [26]. In our case, since we are primarily interested in the segmentation of individual cells in 3D, near-isotropic resolution is more appropriate.

Here we describe a novel microscopy technique that provides video-rate, multiplane, optically sectioned imaging over large FOVs on the millimeter scale. Our technique, called Multi-Z confocal microscopy, is based on three main ideas. The first is to combine high-NA detection with low-NA illumination. The former leads to high signal collection efficiency; the latter leads to axially extended illumination over a large range of Z depths. The second idea is to detect multiple signals from this extended depth range using multiple confocal pinholes that are axially distributed (similar to the technique in [27], though over a much larger scale). The pinholes are reflecting, so that signal rejected by one pinhole is sent to the next pinhole, and so forth. In this manner, no signal is lost, and signal collection efficiency remains high (a reflecting pinhole has been used previously, though in the context of two-photon microscopy [28]). The third idea is to exploit the benefits obtained from our larger confocal probe volumes, namely larger signals and avoidance of oversampling at cellular resolution, to scan over much larger fields of view (FOVs) than provided by standard confocal microscopes, thus optimizing our Multi-Z microscope for fast, large-scale imaging of cell populations.

2. MULTI-Z PRINCIPLE

A schematic of our experimental setup is shown in Fig. 1(a). In practice, our instrument resembles a standard confocal microscope, though with differences in both the illumination and detection optics. To achieve low-NA illumination, we significantly underfill the back aperture of our microscope objective (MO) by inserting an afocal beam compressor in the excitation laser path, which results in a highly axially elongated illumination beam in the sample. With $NA_{ill} \approx 0.1$, the axial extent on the illumination focus is of the order of 100 μm. The fluorescence from the sample, in turn, is epicollected through the full aperture of the same MO, which ensures both maximized fluorescence collection efficiency and a detection depth of field much shorter than the illumination axial depth [see Fig. 1(b)]. The fluorescence is then routed to not one but several pinholes (here four), each conjugate to different depths separated by Δz (here 25 μm) within the illumination profile. The size of the pinholes is adjusted to be approximately $M\delta x$, where δx is the transverse illumination width

and M is the magnification from the sample to the pinholes (here $M = 62.5$). In the image space, the separation between the pinholes ΔZ is given by approximately $M^2\Delta z$. Because of its quadratic dependence on M, this separation is in the range of several centimeters even though Δz is in the range of microns, making the pinhole layout particularly convenient to build (as opposed to the more restricted implementation involving high-NA illumination and close-packed micromachined reflectors [27]). We note that downstream channels are subject to a small amount of screening from the pinholes in the upstream channels. An evaluation of this minor effect is discussed in Supplement 1.

To evaluate the resolution of our microscope, we imaged sub-diffraction-sized beads over a 200 μm axial range about the MO focal plane. Using a 10 × objective, we achieved for each detection channel a resolution of $\delta x = 2.6$ μm and $\delta z = 15$ μm in the transverse and axial dimensions, respectively [Fig. 1(c)]. Note that this compromise in resolution was purposefully chosen to facilitate high-speed imaging over large FOVs. Such 3D resolution is easily adequate to resolve individual cells, such as neurons in brain tissue, while avoiding problems associated with oversampling and the unnecessary processing of massive amounts of data [29]. The resultant bead signal simultaneously recorded by the four detection channels clearly demonstrates the multiplane capability of our approach [see Fig. 1(d)]. As expected, the four curves are similar and axially shifted by $\Delta z = 25$ μm, thus illustrating confocal detection over 100 μm. The slightly broader and lower amplitude responses associated with the first and last detection channels arise from the axial rolloff of our Gaussian–Lorentzian illumination beam away from its nominal focus, as detailed in Supplement 1.

As an example demonstration, we imaged a fixed sample of Aspergillus conidiophores, a common mold. Figure 1(e) shows the four simultaneously acquired images from the shallowest ($z = -37.5$ μm) to the deepest plane ($z = +37.5$ μm). Different features and the branching of the hydrae are clearly visible in these images, demonstrating the simultaneous multiplane acquisition and optical sectioning capabilities of our microscope over a large FOV, here 1.2 × 1.2 mm^2. A side-by-side comparison of a stack acquired simultaneously by Multi-Z microscopy and sequentially by sample-stage translation with data only from a single pinhole is provided in Supplement 1.

3. HIGH-SPEED VOLUMETRIC IMAGING

Because Multi-Z confocal microscopy provides volumetric imaging without the need for axial scanning, its speed is limited only by the mechanism for transverse 2D scanning. In our case, we use standard resonant-nonresonant galvanometric scanning (see Section 6, Methods) to achieve video-rate imaging, easily fast enough to monitor the dynamics of cell activity reporters such as the calcium sensor GCaMP6. In particular, we demonstrate the speed capacity of our system by monitoring large-scale *in vivo* neuronal activity in different organisms.

A. Whole Animal Study: Caenorhabditis elegans

We first performed imaging of *C. elegans* expressing both NLSmCherry, targeted to nuclei, and GCaMP6s. Adult worms are typically 500–800 μm long and 100 μm wide, which makes

them difficult to image entirely with a conventional confocal microscope. As a result, only young specimens or the head ganglia are usually imaged. However, our microscope readily captured full 3D volumes of multiple worms embedded in agarose gel, here up to four. Using two-color illumination and interleaved acquisition (see Section 6, Methods) we were able to simultaneously detect the neurons and monitor their activity. Figure 2(a) displays the extended depth of field (EDOF) image of the nuclei obtained by summing the intensity of the four channels. Numerous neurons of the worms, from the densely packed head ganglia to the tail, are visible. Since the calcium activity is simultaneously recorded, the active neurons can be spatiotemporally resolved in 4D [see Fig. 2(b)]. Such a rendering would not be possible with conventional confocal microscopy, which is limited to single-plane imaging over typically much smaller FOVs. Moreover, our approach enabled us to perform volumetric imaging of moving specimens (see Visualization 1). Because of the agarose gel, the worm was constrained to rotations only, but our approach could be extended to freely moving worms as well. From the same acquisition, the Ca^{2+} activity of the 42 detected ventral neurons of a selected worm (blue-dashed rectangle) was monitored at 7.5 Hz for 200 s [Fig. 2(d)]. The corresponding Ca^{2+} traces are shown in Fig. 2(e), where different subsets of neurons reveal clearly correlated and anticorrelated activity associated to forward and backward motion, in agreement with previous observations [11,26].

To image densely packed regions such as head ganglia, a higher transverse resolution is preferable. This could be obtained while maintaining the same distance Δz between imaging planes by simply switching the MO (20×) and two relay lenses to maintain a constant M (see Section 6, Methods). In this new configuration, we imaged the head ganglion of a worm (zoomed to 300 × 300 × 100 μm^3) at 30 Hz. Figure 2(f) shows an overlay of the temporal standard deviation of the Ca^{2+} signals, where color corresponds to depth. Neurons from different depths are clearly distinguishable in this densely populated region. Note that due to internal motion, the worm intestine is also highlighted when we compute the standard deviation. In total, 32 neurons are identified over a duration of 1000 s, and their Ca^{2+} traces are presented as a heat map in Fig. 2(g). Our acquisition speed was amply sufficient to record even the fastest Ca^{2+} dynamics (see also Visualization 2).

B. Mouse Brain

More challenging is the demonstration of *in vivo* neuronal imaging in mammalian brains. For this, we performed Ca^{2+} imaging in a mouse brain expressing GCaMP6f, requiring both fast imaging, at least 15 Hz, and optical sectioning to reject extraneously scattered light. We focused in particular on the hippocampus, a subcortical region of the brain (see Section 6, Methods). During imaging, the mice were awake and head-fixed, and no sensory stimulus was applied.

We recorded the spontaneous Ca^{2+} activity of neurons within a 1200 × 1200 × 100 μm^3 volume at 30 Hz, the fastest rate currently achievable with our system for this FOV. Though the labeling was confined to an area smaller than our FOV, the EDOF images (i.e., Z projections) reveal a large population of neurons [see Fig. 3(a)]. Higher resolution images of smaller regions of interest were also obtained by reducing the FOV while keeping the same acquisition speed and number of pixels, allowing the details of individual cells to become

clearer (see inset and Visualization 4). The benefits of simultaneous, multiplane acquisition are apparent in Fig. 3(b), where different neurons are revealed in different imaging planes. Using a constrained non-negative matrix factorization algorithm (CNMF) [30], 90, 264, 312, and 260 neurons were separately identified in each plane, from deepest to shallowest, respectively, resulting in a total number of 926 neurons. Owing to the intentional partial overlap of the image planes [see Fig. 1(d)], some of these identifications are expected to be redundant. Indeed, similar processing applied to the EDOF images pared back these identifications to a total of 826 independent neurons, indicating that the overlap-induced crosstalk was approximately 12% [Fig. 3(a) and Visualization 3]. The corresponding extracted Ca^{2+} traces, recorded over 66 s, are shown in Figs. 3(c) and 3(d) for a magnified view. These results illustrate the capacity of our system to provide an adequate SNR for neuronal segmentation in large, relatively dense populations at video-rate speeds.

4. AUGMENTED VOLUMETRIC IMAGING

Our microscope was designed to provide multiplane acquisition over an axial range of about 100 μm. In the event that a larger axial range is desired, several strategies can be considered. The first, and simplest, is to further extend the range of the illumination focus by further underfilling the back aperture of the MO. In this case, the detection channels can be spread more sparsely along the illumination profile, reducing the detection fill factor and hence the spatial overlap of neighboring detection probe volumes. Alternatively, to maintain the same fill factor, the number of channels (and pinholes) can be increased. Such a simple solution, however, would incur a loss in transverse spatial resolution. For example, a doubling of the axial range would lead to a worsening of the transverse resolution by a factor of $\sqrt{2}$.

Yet another strategy that does not impair transverse resolution involves the use of a mechanism to rapidly change focal depths. Example mechanisms are an electrically tunable lens (ETL) [31], an acoustic gradient lens [32,33], or a deformable mirror [5]. In our case, we demonstrated the augmentation of our axial range with an ETL (Optotune VIS-EL-10-30-C), which we inserted in the vicinity of the pupil plane between the scanning mirrors and the MO. By controlling the focal strength of the ETL, we thus axially translated both the illumination and detection foci by up to 150 μm, while incurring little change in the magnification and resolution of our system. In particular, a square-wave control voltage was applied to the ETL at half the microscope frame rate, leading to interleaved stack acquisition that doubles the effective axial range of our microscope, though at the cost of halving our net acquisition speed.

As an example demonstration, we imaged a fixed mouse brain with fluorescein isothiocyanate (FITC)-labeled vasculature. In a two-step acquisition process, we recorded eight frames in total, four from each axial position of the ETL, leading to an overall imaging volume of $1200 \times 1200 \times 250\ \mu m^3$ acquired at a net speed of 15 Hz. Figure 4(b) displays a resulting volume projection with color-coded depth, revealing both larger vessels that span the full axial extent of the recorded volume and smaller vessels visible only in individual frames. These preliminary results further demonstrate versatility of our microscope in providing large-scale imaging.

5. SUMMARY

In summary, we have developed a generalized version of confocal microscopy that provides simultaneous multiplane imaging over large FOVs while remaining fast—here, video rate. Advantages of our system are that it is highly light efficient, for two reasons. First, it makes full use of the detection NA and incurs no loss upon signal detection through reflecting pinholes, thus maximizing signal collection efficiency. Second, whereas in a standard confocal microscopy the illumination light produces only a single image plane at a time, in Multi-Z confocal microscopy the *same* illumination light is repeatedly utilized to produce multiple image planes at a time. This makes more efficient usage of the laser excitation power and, concomitantly, for the acquisition of equal image stacks, reduces the deleterious effects associated with this excitation power, such as photobleaching, photodamage, etc. This second excitation efficiency advantage is expected to scale with the number of pinholes.

Other advantages of Multi-Z microscopy are that the system requires no scan pre-calibration and no image postprocessing. Indeed, the images shown here were not postprocessed in any way, save for image registration to correct for sample dither, illustrating the robustness of our system against motion artifacts which can easily be monitored in all three dimensions. On the other hand, postprocessing could be envisaged, such as 3D deconvolution, as facilitated by the direct acquisition of volumetric image data. Also, our approach is robust against axial motion artifacts that may arise, for example, from blood flow or animal breathing, which is a common problem in *in vivo* applications. While in conventional confocal microscopy axial motion can lead to total loss of the signal, here the signal simply appears in a different channel.

Still other advantages are that our system is readily scalable to a greater number of imaging planes, with no speed penalty in principle, by simply adding pinholes and detectors, or to an augmentation of axial range with minimal penalty in transverse resolution. Moreover, it is versatile in that it is amenable to multicolor imaging (e.g., two-color here), and M and/or Δz can be adjusted with only minor optical modifications. For example, since $\Delta Z = M^2 \times \Delta z$, one can adjust the distance between the imaging planes Δz by simply tuning the total magnification of the system M, or alternatively by tuning the physical distance between the pinholes ΔZ. In our case, Δz was adjusted so that the confocal detection volumes filled the axial extent of the illumination beam and there was no gap between image planes. Other geometries are, of course, possible.

The simplicity and ease of use of our system should make it attractive for general biomedical research applications.

6. METHODS

A. Hardware Setup

Light from a blue (488 nm/80 mW, Omicron PhoxX) or yellow–green laser (561 nm/50 mW, Vortran Stradus) was scanned by a pair of galvanometric mirrors (CRS 8 kHz, Cambridge Technology) and relayed by lenses to fill only a fraction of the back pupil aperture of

the MO (Optem LWD 10×, NA 0.45 or Olympus XLUMPLFLN-W 20 × NA = 0.95). The underfilling of the pupil results in low NA illumination ($NA_{ill} \approx 0.1$) that provides an axially extended focus in the focal plane of the MO. The fluorescence signal was epidetected by the full NA of the same MO, ensuring maximal collection efficiency and constrained axial resolution. The fluorescence signal was then descanned and isolated with a dichromatic mirror (403/497/574, Edmund Optics) and two notch filters (OD4 488NM, Edmund Optics and NF03-561E-25, Semrock). After being relayed and further magnified, the fluorescence was detected by four reflecting pinholes (d = 300 μm, National Aperture) that were axially distributed. The separation between consecutive pinholes was 10 cm, which, given the magnification of the system (M 62.5 ×), corresponds to a separation of Δz = 25 μm in the object space. The signals from the four photodetectors (MicroFC-SMA-30020, SensL) positioned behind the pinholes were amplified by custom-built voltage amplifiers and digitized by a high-speed four-channel field-programmable gate array (FPGA) board (PXI-7961R, National Instruments). The setup was controlled from a dual-CPU workstation, and the experiments were conducted using Scanimage [34] microscope control software.

B. Fixed Samples' Experiments

Point spread function (PSF) measurements were performed using 0.5 μm fluorescent beads (TetraSpeck, ThermoFisher T14792) mounted on a glass slide. We used a commercially available Aspergillus conidiophores glass slide (Carolina Biological Supply Co. 297872). An average laser output power of 3 mW was used for these experiments.

C. Caenorhabditis elegans Preparation

C. elegans strains were cultivated at 20°C following standard procedures (on nematode growth media (NGM) agar seeded with Escherichia coli OP50 as a food source). All imaging experiments were performed on young-adult hermaphrodites using the transgenic strain QW1217 (zfIs124[Prgef-1::GCaMP6s]; otIs355[Prab-3::NLS::tagRFP]) expressing panneuronal GCaMP and nuclear-localized red fluorescent protein (RFP) in all neurons in the worm. Worms were partially immobilized for imaging by following a hydrogel encapsulation protocol [35]. In brief, worms were placed into a droplet of solution consisting of 10 polyethylene glycol diacrylate (PEG-DA) and 0.1% Igracure. The droplet containing the worms was then hardened by a minute-long exposure to UV light, which crosslinked the solution into a gel, preventing gross movement of the worms. An average laser output power of 5 mW was used for these experiments.

D. Mouse Preparation and Imaging

All animal procedures were in accordance with the National Institutes of Health Guide for the care and use of laboratory animals and approved by the Boston University Institutional Animal Care and Use Committee. Female C57BL/6 mice (n = 2, Taconic; Hudson, NY), 8–12 weeks old at the time of surgery, were first injected with AAV9-Syn-GCaMP6f.WPRE.SV40 virus obtained from the University of Pennsylvania Vector Core (titer ~6e12GC/ml). 250 nL of virus was stereotaxically injected into the CA1 region (AP: −2 mm, ML: 1.4 mm, DV: −1.6 mm) using a 10 nL syringe (World Precision Instruments) fitted with a 33 gauge needle (NF33BL; World Precision Instruments), at a speed of 40 μL/min controlled by a microsyringe pump (UltraMicroPump3–4; World

Precision Instruments). Upon complete recovery, animals were surgically implanted with custom-imaging windows, which consisted of a stainless steel cannula (OD: 0.317 cm, ID: 0.236 cm, height 2 mm) adhered to a circular coverslip (size 0; OD: 3 mm) with a UV-curable optical adhesive (Norland Products). After careful aspiration of the over-lying cortical tissue, using the corpus callosum as an anatomical guide, the imaging window was placed above the CA1 viral injection site. During the same surgery, a custom aluminum head-plate was attached to the skull anterior to the imaging cannula for head fixation during imaging. Animals were imaged beginning 4 weeks later to allow for full expression of GCamp6f. Prior to imaging for the first time, animals were also habituated to a custom-mount head fixation apparatus over several sessions as previously described [36]. An average laser output power of 5 mW was used for these experiments. Imaging sessions lasted typically 15–20 min.

E. Fixed-Brain Preparation

Before extracting a mouse brain, a cardiac perfusion with heparinized saline followed by FITC-albumin-gelatin was performed. After extraction, the brain was immersed in a 4% paraformalde-hyde (PFA) solution for 6 h and then in a phosphate-buffered saline (PBS) solution for 3 days. Subsequently, the solution was replaced by distilled water with 0.5% alpha-thioglycerol and increasing amounts of fructose, 20%, 40%, 60%, 80%, and finally 100%.

F. Image Processing and Data Analysis

Motion correction was performed using the Moco plugin [37] in ImageJ. Data analysis was carried out using custom scripts in Matlab (MathWorks) for the *C. elegans* experiments and using a constrained non-negative matrix factorization algorithm for the mice experiments [30]. Redundant neurons were identified by comparing the results obtained when the algorithm was applied to the images from the individual channels to the results obtained directly from the EDOF images. To extract $\Delta F/F_0$, we computed $\Delta F/F_0(t) = 100 \times (F(t) - F_0)/F_0$, F_0 being the mean fluorescence intensity of each trace.

Supplementary Material

Refer to Web version on PubMed Central for supplementary material.

Acknowledgment.

We thank Timothy Weber, Jean-Marc Tsang, and Sheng Xiao for technical help and helpful discussions. We thank the BU Neurophotonics Center for general support and especially Kivilcim Kilic for providing the fixed brain sample. See Supplement 1 for supporting content.

Funding.

National Institutes of Health (NIH) (R21-EY027549); Wallace H. Coulter Foundation (WHCF).

REFERENCES

1. Ji N, Freeman J, and Smith SL, “Technologies for imaging neural activity in large volumes,” Nat. Neurosci 19, 1154–1164 (2016). [PubMed: 27571194]

2. Yang W and Yuste R, “In vivo imaging of neural activity,” Nat. Methods 14, 349–359 (2017). [PubMed: 28362436]
3. Botcherby EJ, Juškaitis R, Booth MJ, and Wilson T, “Aberration-free optical refocusing in high numerical aperture microscopy,” Opt. Lett 32, 2007–2009 (2007). [PubMed: 17632625]
4. Chen T-H, Ault J, Stone H, and Arnold C, “High-speed axial-scanning wide-field microscopy for volumetric particle tracking velocimetry,” Exp. Fluids 58, 41 (2017).
5. Shain WJ, Vickers NA, Goldberg BB, Bifano T, and Mertz J, “Extended depth-of-field microscopy with a high-speed deformable mirror,” Opt. Lett 42, 995–998 (2017). [PubMed: 28248351]
6. Dowski ER and Cathey WT, “Extended depth of field through wave-front coding,” Appl. Opt 34, 1859–1866 (1995). [PubMed: 21037731]
7. Quirin S, Peterka DS, and Yuste R, “Instantaneous three-dimensional sensing using spatial light modulator illumination with extended depth of field imaging,” Opt. Express 21, 16007–16021 (2013). [PubMed: 23842387]
8. Blanchard PM and Greenaway AH, “Simultaneous multiplane imaging with a distorted diffraction grating,” Appl. Opt 38, 6692–6699 (1999). [PubMed: 18324206]
9. Dalgarno PA, Dalgarno HI, Putoud A, Lambert R, Paterson L, Logan DC, Towers DP, Warburton RJ, and Greenaway AH, “Multiplane imaging and three dimensional nanoscale particle tracking in biological microscopy,” Opt. Express 18, 877–884 (2010). [PubMed: 20173908]
10. Abrahamsson S, Chen J, Hajj B, Stallinga S, Katsov AY, Wisniewski J, Mizuguchi G, Soule P, Mueller F, Darzacq CD, and Darzacq X, “Fast multicolor 3D imaging using aberration-corrected multifocus microscopy,” Nat. Methods 10, 60–63 (2012). [PubMed: 23223154]
11. Prevedel R, Yoon Y-G, Hoffmann M, Pak N, Wetzstein G, Kato S, Schrödel T, Raskar R, Zimmer M, Boyden ES, and Vaziri A, “Simultaneous whole-animal 3D imaging of neuronal activity using light-field microscopy,” Nat. Methods 11, 727–730 (2014). [PubMed: 24836920]
12. Pégard NC, Liu H-Y, Antipa N, Gerlock M, Adesnik H, and Waller L, “Compressive light-field microscopy for 3D neural activity recording,” Optica 3, 517–524 (2016).
13. Huisken J, Swoger J, Del Bene F, Wittbrodt J, and Stelzer EH, “Optical sectioning deep inside live embryos by selective plane illumination microscopy,” Science 305, 1007–1009 (2004). [PubMed: 15310904]
14. Bouchard MB, Voleti V, Mendes CS, Lacefield C, Grueber WB, Mann RS, Bruno RM, and Hillman EM, “Swept confocally-aligned planar excitation (scape) microscopy for high-speed volumetric imaging of behaving organisms,” Nat. Photonics 9, 113–119 (2015). [PubMed: 25663846]
15. Xiao S, Tseng H-A, Gritton H, Han X, and Mertz J, “Video-rate volumetric neuronal imaging using 3D targeted illumination,” Sci. Rep 8, 7921 (2018). [PubMed: 29784920]
16. Amir W, Carriles R, Hoover EE, Planchon TA, Durfee CG, and Squier JA, “Simultaneous imaging of multiple focal planes using a two-photon scanning microscope,” Opt. Lett 32, 1731 (2007). [PubMed: 17572762]
17. Cheng A, Goncalves JT, Golshani P, Arisaka K, and Portera-Cailliau C, “Simultaneous two-photon calcium imaging at different depths with spatiotemporal multiplexing,” Nat. Methods 8, 139–142 (2011). [PubMed: 21217749]
18. Kong L, Tang J, Little JP, Yu Y, Lämmermann T, Lin CP, Germain RN, and Cui M, “Continuous volumetric imaging via an optical phase-locked ultrasound lens,” Nat. Methods 12, 759–762 (2015). [PubMed: 26167641]
19. Otsu Y, Bormuth V, Wong J, Mathieu B, Dugué GP, Feltz A, and Dieudonné S, “Optical monitoring of neuronal activity at high frame rate with a digital random-access multiphoton (ramp) microscope,” J. Neurosci. Methods 173, 259–270 (2008). [PubMed: 18634822]
20. Nadella KNS, Roš H, Baragli C, Griffiths VA, Konstantinou G, Koimtzis T, Evans GJ, Kirkby PA, and Silver RA, “Random-access scanning microscopy for 3D imaging in awake behaving animals,” Nat. Methods 13, 1001–1004 (2016). [PubMed: 27749836]
21. Yang W, Miller J-EK, Carrillo-Reid L, Pnevmatikakis E, Paninski L, Yuste R, and Peterka DS, “Simultaneous multi-plane imaging of neural circuits,” Neuron 89, 269–284 (2016). [PubMed: 26774159]

22. Lu R, Sun W, Liang Y, Kerlin A, Bierfeld J, Seelig JD, Wilson DE, Scholl B, Mohar B, Tanimoto M, and Koyama M, "Video-rate volumetric functional imaging of the brain at synaptic resolution," Nat. Neurosci 20, 620–628 (2017). [PubMed: 28250408]
23. Song A, Charles AS, Koay SA, Gauthier JL, Thiberge SY, Pillow JW, and Tank DW, "Volumetric two-photon imaging of neurons using stereoscopy (vtwins)," Nat. Methods 14, 420–426 (2017). [PubMed: 28319111]
24. Roider C, Piestun R, and Jesacher A, "3d image scanning microscopy with engineered excitation and detection," Optica 4, 1373–1381 (2017).
25. Shain WJ, Vickers NA, Li J, Han X, Bifano T, and Mertz J, "Axial localization with modulated-illumination extended-depth-of-field microscopy," Biomed. Opt. Express 9, 1771–1782 (2018). [PubMed: 29675318]
26. Schrödel T, Prevedel R, Aumayr K, Zimmer M, and Vaziri A, "Brain-wide 3D imaging of neuronal activity in Caenorhabditis elegans with sculpted light," Nat. Methods 10, 1013–1020 (2013). [PubMed: 24013820]
27. Yang C, Shi K, Zhou M, Zheng S, Yin S, and Liu Z, "Z-microscopy for parallel axial imaging with micro mirror array," Appl. Phys. Lett 101, 231111 (2012).
28. Hu Q, Li P, Xiong Y, Wang Y, Lv X, and Zeng S, "Simultaneous two-plane, two-photon imaging based on spatial multiplexing," Opt. Lett 43, 4598–4601 (2018). [PubMed: 30272692]
29. Weisenburger S, Prevedel R, and Vaziri A, "Quantitative evaluation of two-photon calcium imaging modalities for high-speed volumetric calcium imaging in scattering brain tissue," bioRxiv (2017), p. 115659.
30. Pnevmatikakis EA, Soudry D, Gao Y, Machado TA, Merel J, Pfau D, Reardon T, Mu Y, Lacefield C, Yang W, and Ahrens M, "Simultaneous denoising, deconvolution, and demixing of calcium imaging data," Neuron 89, 285–299 (2016). [PubMed: 26774160]
31. Grewe BF, Voigt FF, van 't Hoff M, and Helmchen F, "Fast two-layer two-photon imaging of neuronal cell populations using an electrically tunable lens," Biomed. Opt. Express 2, 2035–2046 (2011). [PubMed: 21750778]
32. Olivier N, Mermillod-Blondin A, Arnold CB, and Beaurepaire E, "Two-photon microscopy with simultaneous standard and extended depth of field using a tunable acoustic gradient-index lens," Opt. Lett 34, 1684–1686 (2009). [PubMed: 19488148]
33. Duocastella M, Vicidomini G, and Diaspro A, "Simultaneous multiplane confocal microscopy using acoustic tunable lenses," Opt. Express 22, 19293–19301 (2014). [PubMed: 25321014]
34. Pologruto TA, Sabatini BL, and Svoboda K, "Scanimage: flexible software for operating laser scanning microscopes," Biomed. Eng. online 2, 13 (2003). [PubMed: 12801419]
35. Burnett K, Edsinger E, and Albrecht DR, "Rapid and gentle hydrogel encapsulation of living organisms enables long-term microscopy over multiple hours," Commun. Biol 1, 73 (2018). [PubMed: 30271954]
36. Mohammed AI, Gritton HJ, Tseng H-A, Bucklin ME, Yao Z, and Han X, "An integrative approach for analyzing hundreds of neurons in task performing mice using wide-field calcium imaging," Sci. Rep 6, 20986 (2016). [PubMed: 26854041]
37. Dubbs A, Guevara J, and Yuste R, "moco: Fast motion correction for calcium imaging," Front. Neuroinf 10, 6 (2016).

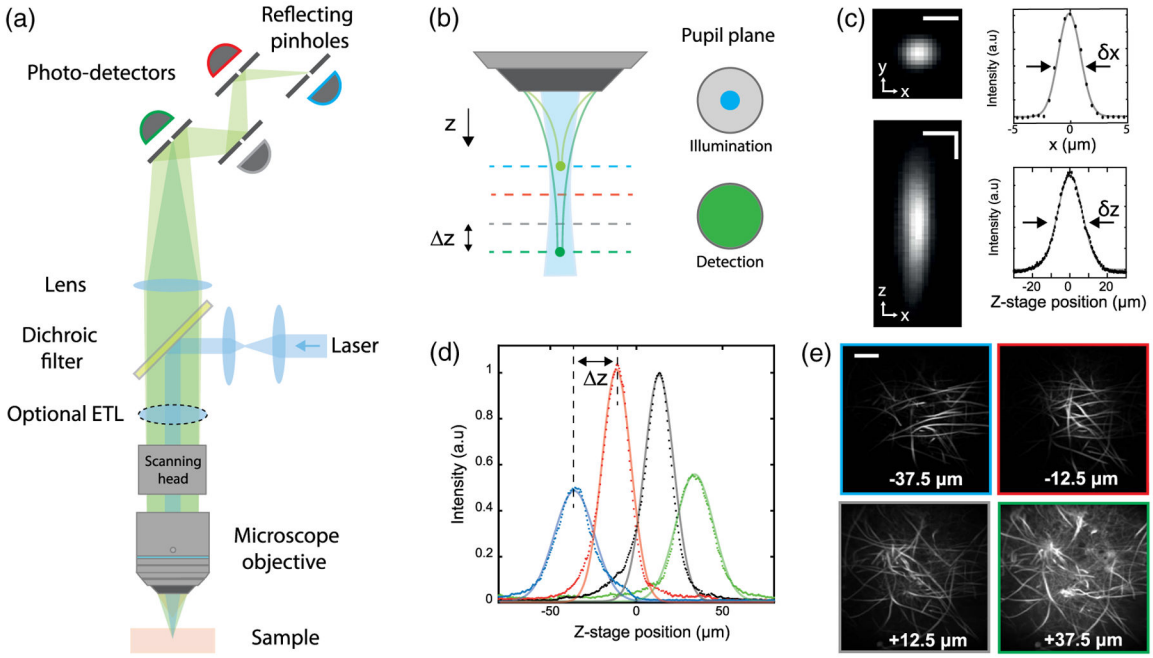

Fig. 1.

Multi-Z confocal microscopy. (a) Simplified schematic of the experimental setup. The multiplane detection unit comprises a series of axially distributed reflecting pinholes, each probing a different depth within the sample. (b) Axially extended illumination is obtained by underfilling the back aperture of the MO. The full NA of the MO is used for detection. (c) Transverse (*xy*) and axial (*xz*) PSF measured with a subdiffraction size bead, and associated *x* and *z* profiles. Horizontal scale bar, 5 μm. Vertical scale bar, 10 μm. (d) Bead signal recorded by each detection channel at different *z* positions of the stage. Continuous lines correspond to Lorentzian fits. (e) Different imaging planes simultaneously acquired of Aspergillus conidiophores. Scale bar, 200 μm.

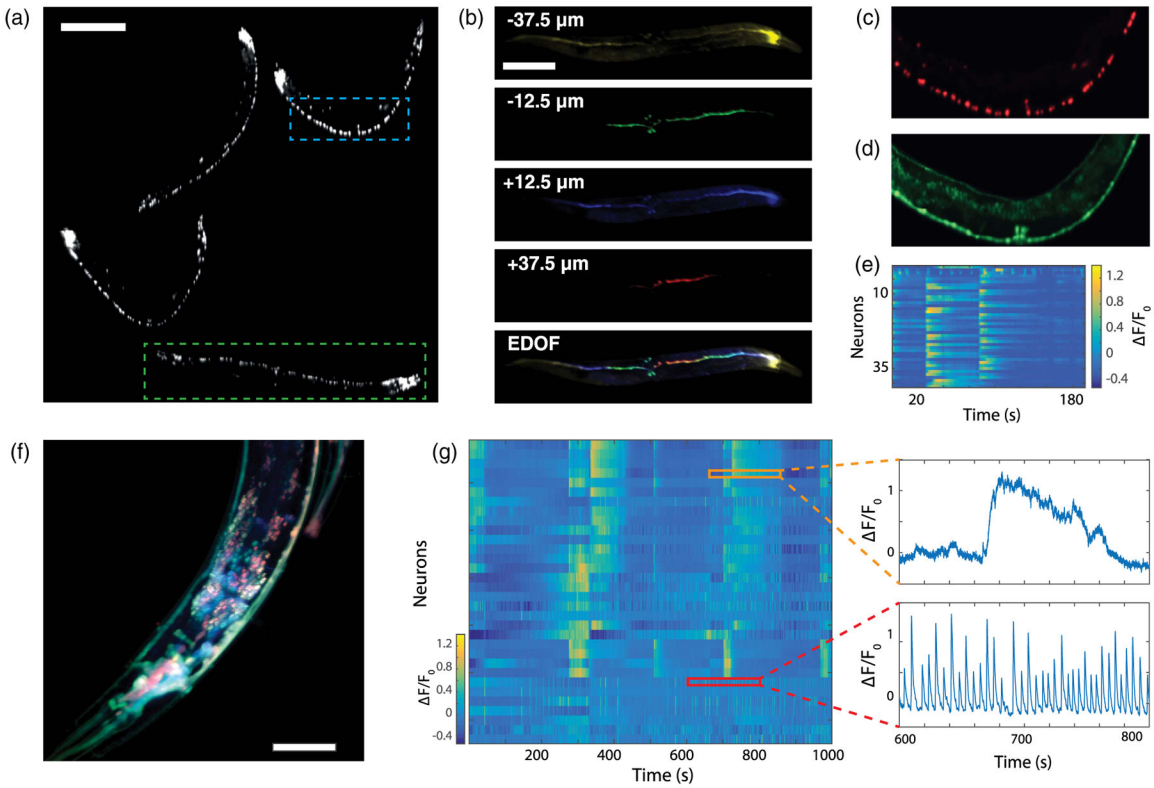

Fig. 2.

In vivo volumetric imaging of *C. elegans*. (a) Extended depth of field image showing the nuclei marked with NLSmCherry of four different worms in the FOV. 1024 × 1024 pixels; scale bar, 200 µm. (b) Simultaneous imaging of a single worm [green rectangle in (a)] at different depths and the resulting volumetric rendering. Scale bar, 200 µm. (c, d) Close up view [blue rectangle in(a)], showing the nuclei (in red) and the neurons displaying activity (in green). (e) Activity of the 42 neurons identified in (d). (f) Standard deviation of the calcium activity recorded in the head ganglion of a worm in each imaging plane. Each channel is displayed with a different color and in log scale. (see Visualization 2 for a video of intensity variations). 512 × 512 pixels; scale bar, 50 µm. (g) Activity of the 32 neurons identified in (f) and recorded over 1000 s. Each row corresponds to a time-series of an individual neuron, as shown in the insets.

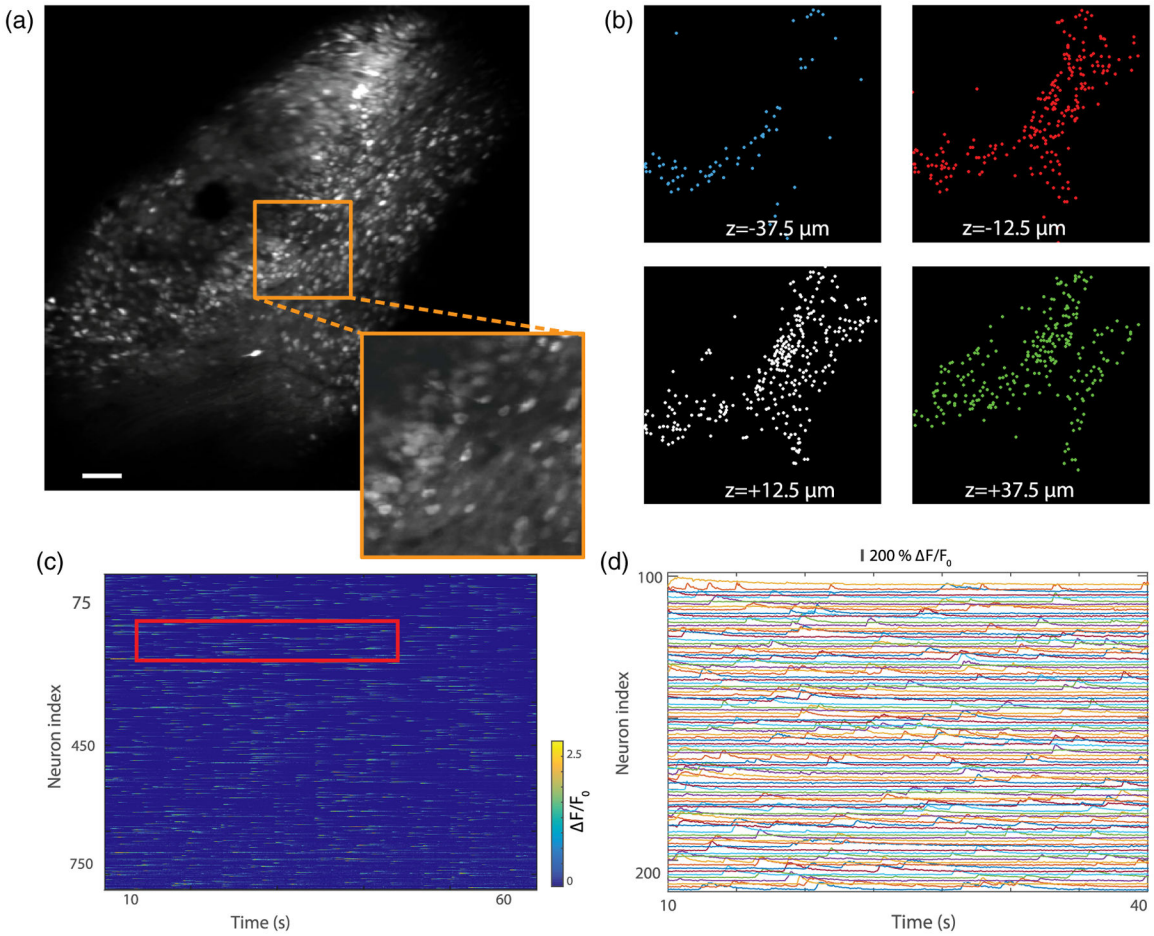

Fig. 3.

Video-rate volumetric Ca^{2+} imaging in mouse brain expressing GCaMP6f (note that viral injection here led to a labeled area somewhat smaller than our FOV). (a) Extended depth of field image recorded in the hippocampus at 30 frames per second and averaged over 20 s (see Visualization 3 for the video). 512 × 512 pixels; scale bar, 100 µm. Inset with 3 × zoom illustrates cellular resolution. (b) Identification of neurons in each image plane using constrained non-negative matrix factorization (overlay with Panel *a* is shown in Supplement 1). (c) Activity of the 826 neurons identified in (a). (d) Magnified view of the neuronal activity traces for the region indicated by the red rectangle in (c).

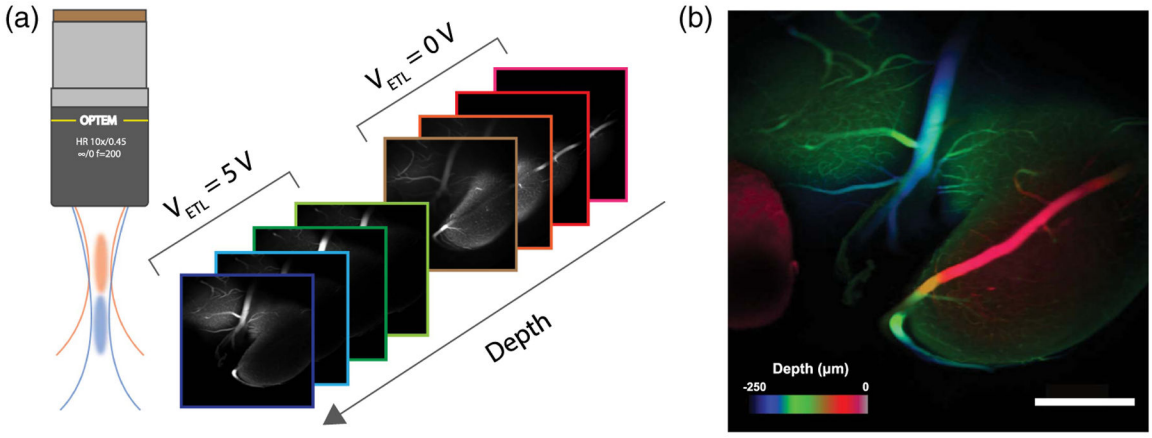

Fig. 4.

Augmented volumetric imaging using an electrically tunable lens controlled by a square-wave voltage V_{ETL}. (a) Multi-Z images obtained for V_{ETL} = 0 and V_{ETL} = 5 V corresponding to a focal shift of 150 μm. (b) Resulting volumetric acquisition of fixed mouse brain vasculature with structures color-coded by depth. 512 × 512 pixels; scale bar 300 μm.